Available online at www.sciencedirect.com
ScienceDirect
International Journal of Heat and Mass Transfer 50 (2007) 530–538
International Journal of HEAT and MASS TRANSFER
www.elsevier.com/locate/ijhmt

Transient flow and heat transfer leading to periodic state in a cavity with inlet and outlet ports due to incoming flow oscillation

S.M. Saeidi [1], J.M. Khodadadi *

Mechanical Engineering Department, Auburn University, 201 Ross Hall, Auburn, AL 36849-5341, USA

Received 14 December 2005; received in revised form 21 July 2006
Available online 29 September 2006

Abstract

A finite-volume-based computational study of transient laminar flow and heat transfer (neglecting natural convection) leading to periodic state within a square cavity with inlet and outlet ports due to an oscillating velocity at the inlet port is presented. The inlet port is placed at the top of the left wall and the outlet port is positioned at the bottom of the right wall of the cavity. The inlet velocity varies sinusoidally with time for a range of dimensionless frequencies ($St = 0.1$, 0.5, 1, 2 and 10). The instantaneous Reynolds number also varies sinusoidally between 100 and 500 and $Pr = 5$. It takes more cycles for the temperature field to reach its periodic state in comparison to the corresponding flow field. For cases with higher Strouhal numbers, it takes more cycles to reach a periodic state. The throughflow stream undergoes cyclic growth and decay. The throughflow is in constant contact with the clockwise rotating primary vortex, which in turn interacts with two rotating vortices on the left wall. A counterclockwise rotating vortex at the top right corner also experiences periodic growth and decay. Minimal heat transfer is consistently observed on the left wall. In contrast, certain segments of the other three walls and the boundary of the throughflow are zones of active heat exchange. For $St = 0.1$, the mean Nusselt numbers on the four walls clearly exhibit large amplitudes of oscillation and periodicity. With $St = 10$, the amplitudes of oscillation on various walls are generally degraded. These behaviors are directly linked to the relation between the period of oscillation and the convection time scale. Regardless of the Strouhal number, heat transfer enhancement in comparison to the steady state case is consistently observed. The best heat transfer rate is realized when the Strouhal number is close to unity. This is the case when the period of the incoming stream resonates with the convection time scale.

1. Introduction

The most common technique for active control of heat transfer in various convection-dominated heat exchange systems is oscillation of the fluid stream and/or a boundary. A simplified model of a heat exchange unit is that of a cavity with one inlet and one outlet port. Many practical problems can be simplified into this model. For instance, mixed convection studies within cavities that contain heat sources [1–4] are of great interest in electronic cooling, ventilation of buildings and design of solar collectors. Simulations of unsteady mixed convection in thermal storage applications have also received a great deal of attention for many decades [5–11]. Other applications (mass transfer in cavities, relaxation tanks employed in petroleum and transformer industries, transient removal of contaminated fluid from cavities and food processing) were also noted by the authors [12], who investigated steady laminar flow and heat transfer within a cavity with inlet and outlet ports. Nine different positions of the outlet port on the right, left, bottom and top wall were studied with inlet Reynolds numbers equal to 10, 40, 100 and 500.

In extending the work of [12], the objective of this study is to investigate the transient and periodic flow and convective heat transfer in a cavity with inlet and outlet ports with an oscillating velocity variation at the inlet port. The effects

* Corresponding author. Tel.: +1 334 844 3333; fax: +1 334 844 3307.
E-mail address: khodajm@auburn.edu (J.M. Khodadadi).
[1] Graduate Student. Currently a Senior Thermal Engineer, Intel Corporation, Assembly Test & Technology Development, Phoenix, AZ, USA.

0017-9310/$ - see front matter © 2006 Elsevier Ltd. All rights reserved.
doi:10.1016/j.ijheatmasstransfer.2006.07.018

Nomenclature

$\overline{Nu}$	instantaneous mean Nusselt number on a given wall, defined by Eq. (8)
$\overline{Nu}_{tot}$	instantaneous total or overall Nusselt number of the system, defined by Eq. (9)
T_{in}	temperature of the fluid at the inlet port, K
T_w	temperature of the wall, K

Greek symbol

Θ	dimensionless temperature, i.e. $(T - T_{in})/(T_w - T_{in})$

Subscripts

b, l, r, t related to the bottom, left, right and top walls

of the Strouhal number and the oscillating Reynolds number are studied. The results will prove very helpful to design of effective systems that might utilize oscillation of velocity to control heat transfer. It should be noted that the scope of this paper also has commonality with results of previous work on resonant heat transfer enhancement in grooved channels [13–15].

2. Problem formulation

The schematic drawing of the system and the coordinates are shown in Fig. 1. The height and width of the cavity are denoted by H and L, respectively. In this study, only a square cavity is considered ($H = L$). The depth of the enclosure perpendicular to the plane of the diagram is assumed to be long. Hence, the problem can be considered to be two-dimensional. Based on the steady results for this problem [12], in order to maximize heat transfer and minimize the pressure drop, the inlet and outlet ports are placed at the top of the left wall and the bottom of the right wall, respectively. The inlet and outlet port widths are equal ($w_i = w_o = w$) and fixed to 15% of the length of the side wall. The velocity at the inlet port is uniform and depends on time:

$$u_{in} = u_m + u_o \sin 2\pi f t, \tag{1}$$

where f is the frequency of the oscillation. Quantities u_m and u_o ($u_m \geqslant u_o$) are the mean and oscillating inlet velocities, respectively. The inlet fluid is maintained at the temperature (T_{in}) different from the remaining walls of cavity (T_w), with $T_w > T_{in}$. The fluid within the enclosure is incompressible and its properties are constant. The flow within the enclosure is assumed to be laminar. The gravity effect (pointing normal to the xy-plane) and viscous dissipation are neglected. The dimensionless form of the governing equations is obtained via introducing dimensionless variables (capitalized letters, Θ and t^*):

$$X = \frac{x}{H}, \quad Y = \frac{y}{H}, \quad U = \frac{u}{u_m}, \quad V = \frac{v}{u_m},$$
$$P = \frac{p}{\rho u_m^2}, \quad \Theta = \frac{T - T_{in}}{T_w - T_{in}}, \quad t^* = \frac{u_m t}{H}. \tag{2}$$

Variables u, v, p and T are the velocity components in the x-, y-directions, pressure and temperature, respectively. The governing equations for continuity, momentum and thermal energy are then written in dimensionless form:

$$\frac{\partial U}{\partial X} + \frac{\partial V}{\partial Y} = 0, \tag{3}$$

$$\frac{\partial U}{\partial t^*} + U\frac{\partial U}{\partial X} + V\frac{\partial U}{\partial Y} = -\frac{\partial P}{\partial X} + \frac{2w}{H}\frac{1}{Re_m}\left(\frac{\partial^2 U}{\partial X^2} + \frac{\partial^2 U}{\partial Y^2}\right), \tag{4}$$

$$\frac{\partial V}{\partial t^*} + U\frac{\partial V}{\partial X} + V\frac{\partial V}{\partial Y} = -\frac{\partial P}{\partial Y} + \frac{2w}{H}\frac{1}{Re_m}\left(\frac{\partial^2 V}{\partial X^2} + \frac{\partial^2 V}{\partial Y^2}\right), \tag{5}$$

$$\frac{\partial \Theta}{\partial t^*} + U\frac{\partial \Theta}{\partial X} + V\frac{\partial \Theta}{\partial Y} = \frac{2w}{H}\frac{1}{PrRe_m}\left(\frac{\partial^2 \Theta}{\partial X^2} + \frac{\partial^2 \Theta}{\partial Y^2}\right). \tag{6}$$

The mean Reynolds number is defined as $Re_m = u_m 2w/\nu$ and the Prandtl number is $Pr = \nu/\alpha$. For $t^* > 0$, the dimensionless form of the boundary conditions can be expressed as follows (note that $w/H = 0.15$):

At the inlet $(X = 0, 0.85 \leqslant Y \leqslant 1)$:

$$U = 1 + \frac{u_o}{u_m}\sin(2\pi \cdot St \cdot t^*), \; V = 0 \quad \text{and} \quad \Theta = 0.$$

On the walls: $U = V = 0, \quad \Theta = 1.$ (7)

At the outlet $(X = 1, 0 \leqslant Y \leqslant 0.15)$:

$$\frac{\partial U}{\partial X} = 0 \quad \text{and} \quad \frac{\partial \Theta}{\partial X} = 0.$$

The Strouhal number that is a dimensionless parameter widely used in study of oscillating fluid flow phenomena is defined as $St = \frac{H \cdot f}{u_m}$. Therefore, Re_m, Pr, St and u_o/u_m are the dimensionless groups that govern this problem. The instantaneous Reynolds number is defined as $Re = \frac{u_{in} 2w}{\nu}$. Thus, the instantaneous Reynolds number varies sinusoidally as the inlet velocity oscillates. For this study, the ratio

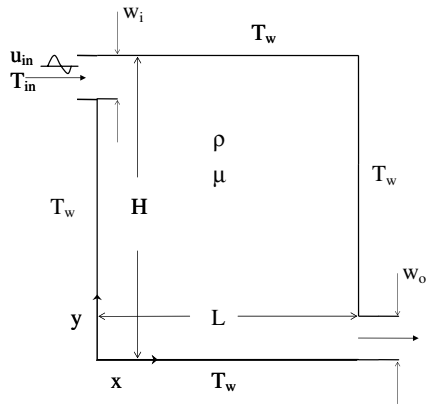

Fig. 1. Schematic diagram of a cavity with inlet and outlet ports.

u_o/u_m is set to 2/3. Thus, with $Re_m = 300$, the instantaneous Reynolds number varies from 100 to 500 (mean value of 300). Five cases are studied with Strouhal numbers of 0.1, 0.5, 1, 2 and 10, respectively and the Prandtl number of the fluid is fixed to 5.

3. Computational details

The governing equations were solved by the finite-volume-method using Patankar's [16] SIMPLE algorithm. A two-dimensional uniformly-spaced staggered grid system was used. Hayase et al.'s [17] QUICK scheme was utilized for the convective terms, whereas the central difference scheme was used for the diffusive terms. In order to keep consistent accuracy over the entire computational domain, a third-order-accurate boundary condition treatment suggested by Hayase et al. [17] was adopted. Details of a grid independence test using six different grid densities (75×75, 100×100, 125×125, 150×150, 175×175 and 200×200) were provided earlier [12] for the steady version of this problem. A 160×160 uniform grid was selected for all cases reported here. The code was recently tested and verified extensively by comparing the results with established forced and buoyancy-driven convection benchmark problems with no throughflow [18]. In extending the applicability of the code to this problem, extensive benchmarking was undertaken in relation to the backward-facing and forward-facing step problems [19]. Specifically, excellent agreement for the computed size and location of the eye of the recirculating vortices against pertinent data of Freitas [20] were established. In addition, the effect of the inlet velocity distribution on the above quantities was discussed.

The steady-state fluid flow and temperature fields for a case with $Re_m = 300$ is treated as the starting field ($t = 0$) in this study. For the unsteady computations, tolerance of the normalized residuals upon convergence is set to 10^{-5} for every time step. The under-relaxation parameters for u, v, and T are all set to 0.6, whereas under-relaxation parameter for pressure correction is set to 0.3. The average number of iterations needed to achieve convergence at every time step were 110, 254, 381, 598 and 1117 for the Strouhal numbers of 0.1, 0.5, 1, 2 and 10, respectively. The three-time-level-method that is a 2nd order implicit scheme is used to approximate the unsteady terms. For a period of oscillation (τ), four different time steps $\Delta t = \tau/72$, $\tau/90$, $\tau/120$ and $\tau/180$ ($St = 10$) were adopted for the time step independence test. After comparing the variations of the mean Nusselt number of the system shown in Fig. 2 ($St = 10$), the time step $\Delta t = \tau/120$ was found small enough to be used for all the cases in this study. All the calculations were performed on a SGI Altix 350 of the Alabama Supercomputer Center (Huntsville, Alabama).

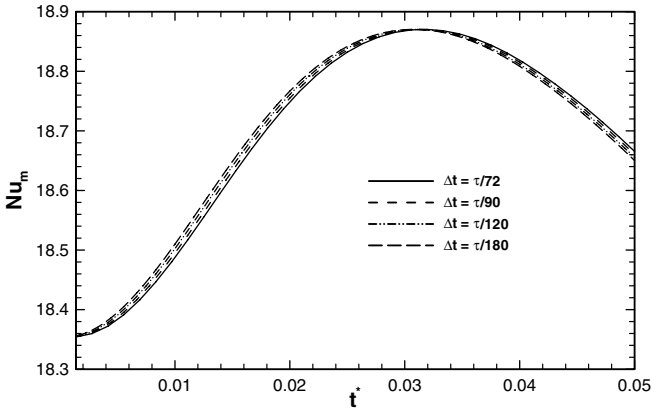

Fig. 2. Comparison of the total mean Nusselt number of the system for various time steps ($St = 10$).

4. Results and discussion

Before presenting the unsteady flow and thermal fields, the behavior of steady velocity and temperature fields [12] are briefly described. The streamlines and temperature contours corresponding to the steady cases with $Re = 100$, 300 and 500 are shown in Fig. 3a and b. The streamlines are shown on the left column (Fig. 3a), whereas the temperature contours are presented on the right column (Fig. 3b), thus allowing one to clearly observe the influence of the complicated flow field on the temperature field. The general features of the flow fields are similar for the three Re numbers studied. It is observed that the streamlines representing the throughflow of the incoming fluid (streamline

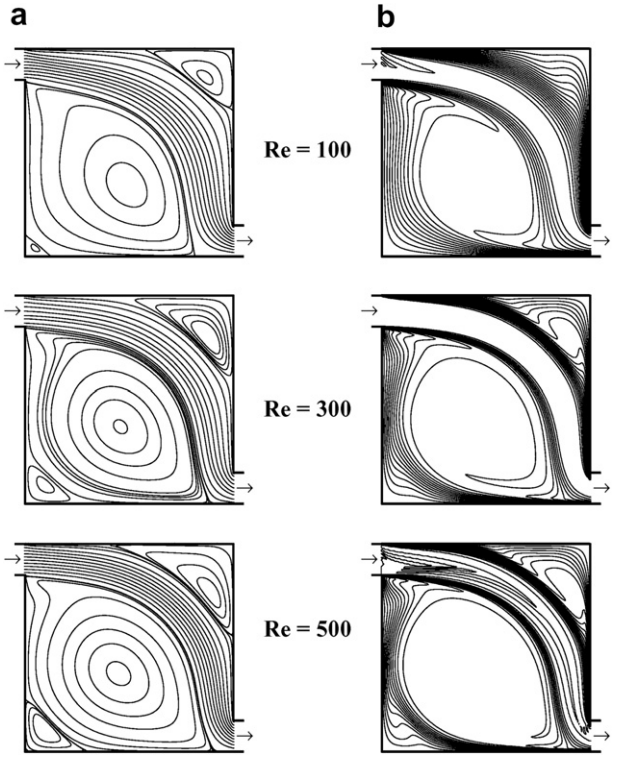

Fig. 3. Dependence of the (a) streamlines and (b) temperature contours for the steady case with $Re = 100$, 300 and 500 (contour level increment of 0.05 for the temperature field).

values of zero and inlet mass flowrate) do not coincide with the two ends of the outlet ports. The area occupied by the clockwise (CW) rotating primary vortex diminishes very little as the Re is increased, whereas a counterclockwise (CCW) rotating vortex next to the top right corner covers a larger portion of the cavity. Another CCW rotating vortex is permanently featured at the bottom left corner with its strength growing with the rise of the Reynolds number. The various flow features are found to be in good agreement with the available flow visualization data [21]. As for the contours of the dimensionless temperature (Θ) shown in Fig. 3b, the value of Θ entering the cavity is zero, whereas on the four solid walls it is one, and the contour levels are incremented by 0.05. The temperature gradient is always marked at the interface of the throughflow stream and the neighboring CW and CCW vortices suggesting intense heat exchange from the fresh incoming fluid to those rotating structures. The core of the primary CW vortex is generally isothermal. Regions of intense fluid temperature gradients are found on both sides of the outlet port. A rise in the value of the Reynolds number brings about steeper fluid temperature gradients next to the left and bottom walls, in addition to greater heat exchange on both sides of the throughflow.

4.1. Transient state of the problem

Starting with the steady state velocity and temperature fields for $Re = 300$, the oscillating incoming velocity of the fluid was imposed at $t = 0$. In response to the imposed inlet velocity condition, the flow and thermal fields will experience a transient adjustment period. After a certain time duration, the fluid flow and temperature fields will reach their respective periodic states. Due to uncoupling of the momentum and energy equations, the fluid flow and temperature fields could reach their respective periodic states at different times. The cycle-to-cycle variations of the fluid flow and temperature fields were quantitatively

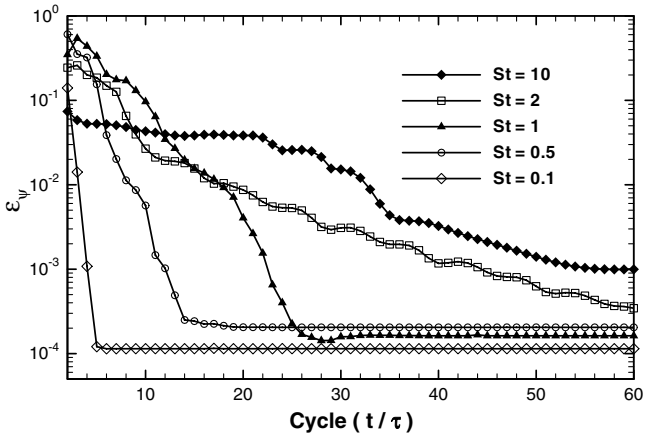

Fig. 4. Cycle-to-cycle changes of the streamline values over the entire domain for different Strouhal numbers.

Table 1
Number of cycles needed to reach the periodic states for fluid flow (N_f) and temperature fields (N_t)

N_f, N_t				
$St = 0.1$	$St = 0.5$	$St = 1$	$St = 2$	$St = 10$
5, 18	13, 21	23, 51	45, 93	57, 107

defined and strictly monitored, exhibiting monotonic decay with time. The measures of the cycle-to-cycle variation of the stream function field for different Strouhal numbers are shown in Fig. 4. It takes a greater number of cycles to achieve the periodic state for cases with high Strouhal numbers in comparison to the cases with smaller St numbers. For all the cases investigated, it takes fewer cycles for the flow field to reach the periodic state than the temperature field. Adopting very stringent criteria [19], the number of cycles needed to reach the periodic state (N_f and N_t) are summarized in Table 1. The difference between N_t and N_f increases as St increases.

Having established the transient nature of the system, the evolution of the periodic flow and temperature fields, the mean Nusselt numbers on the four walls and the time dependence of the overall Nusselt number of the system are discussed next.

4.2. Periodic evolution of the flow field

The periodic flow fields during the thirteenth cycle for the case with $St = 0.5$ are presented for every 30° phase angle in Fig. 5. During the first quarter of the cycle (i.e. $0 \leqslant \alpha \leqslant \pi/2$), as the Reynolds number increases (i.e. $300 \leqslant Re \leqslant 500$), more throughflow enters the cavity. In effect, the area covered by the throughflow is enlarged and the CCW vortex of the top right corner (Fig. 3a) is swept away. The CW rotating primary vortex does not greatly change, however it interacts with two rotating vortices on the left wall. During the second and third quarters of the cycle ($\pi/2 \leqslant \alpha \leqslant 3\pi/2$), when the Reynolds number is decreasing (i.e. $100 \leqslant Re \leqslant 500$) the throughflow diminishes and its coverage area is observed to shrink drastically. Meanwhile the CW rotating primary vortex expands by merging with two small vortices on the left wall. The small vortices were located at the bottom left corner of the cavity (CCW) and right below the inlet port (CW), respectively. During the fourth quarter of the cycle, (i.e. $3\pi/2 \leqslant \alpha \leqslant 2\pi$ and $100 \leqslant Re \leqslant 300$), the primary vortex shrinks with the raising of the Reynolds number and the two small vortices that had previously merged with it reappear on the left wall. A very interesting phenomenon that is observed during the fourth quarter is the penetration of the throughflow into the space between the left wall and the primary CW vortex. The throughflow is observed to touch the middle of the left wall near the end of the cycle. Starting with the second quarter of the cycle, a CCW vortex that is formed next to the top right corner of the cavity strengthens and its region of influence changes as the Reynolds

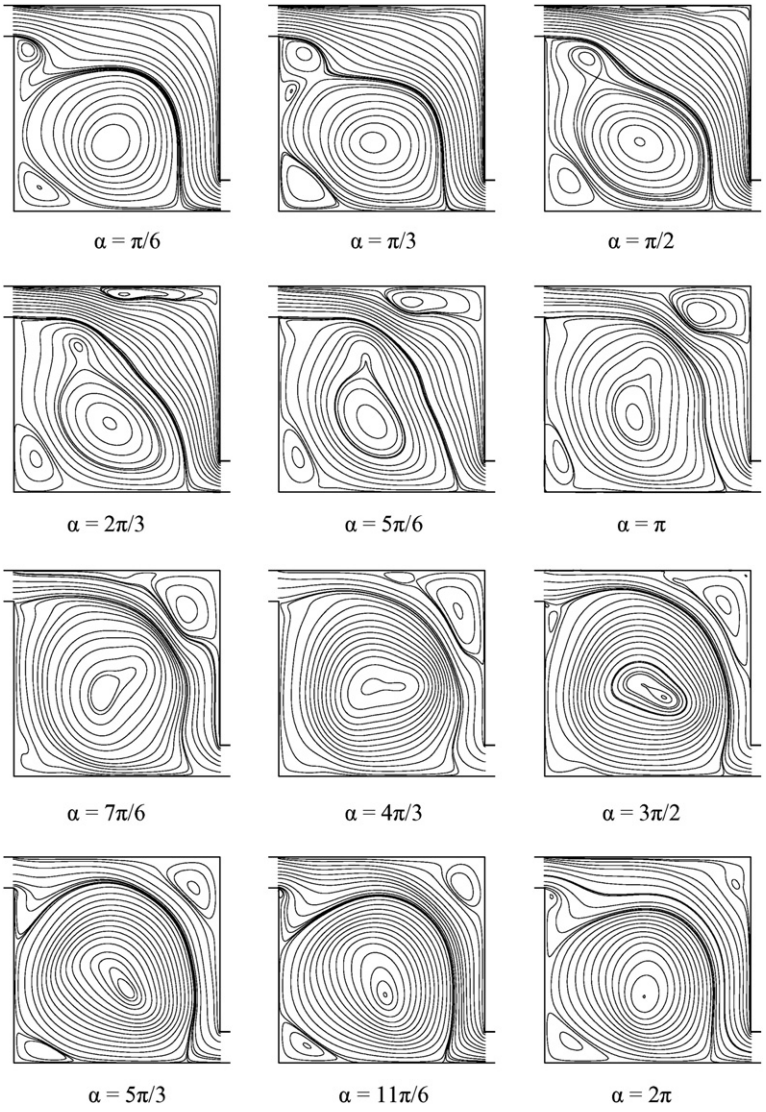

Fig. 5. Periodic evolution of the streamlines for $St = 0.5$ during the 13th cycle for a π/6 phase angle increment.

number reduces. By the end of the fourth quarter, this vortex diminishes and finally, it is washed away by the energetic throughflow.

The evolving multi-vortex structure of the flow field was found to be common to all the cases studied. Comparing the evolution of the flow fields among the various cases, it was observed that the greatest wrinkling and meandering of the throughflow was present for the $St = 1$ case. For the extreme case with $St = 10$, the throughflow and vortices exhibited greatest synchronous behavior during their respective evolving paths.

4.3. Periodic evolution of the temperature field

The contours of dimensionless temperature fields during the 21st cycle for the case with $St = 0.5$ are presented for every 30° phase angle in Fig. 6. There is a one-to-one correspondence between each cavity in this figure to those shown in Fig. 5. In effect, the influence of the complicated flow field on the temperature field can be elucidated. Similar to the temperature contours for the steady cases (Fig. 3b), Θ values are 0 and 1 at the inlet plane and on the four solid walls, respectively, and the contour levels are incremented by 0.05. The temperature within the core of the CW rotating primary vortex remains fairly uniform throughout the cycle, whereas steep temperature gradients are observed on its boundary. Marked heat exchange takes place on the boundary of the primary vortex where it interacts with the evolving throughflow and the two rotating vortices on the left wall. The temperature gradients next to the left wall do not change drastically since the two rotating vortices on this surface are sites of low-speed flow. Similarly, portions of the top and right walls closest to the top right corner do not experience steep variations in temperature gradient due to the frequent presence of a low-speed CCW rotating vortex next to this corner. The most marked temperature gradients and therefore the greatest heat exchange between the fluid

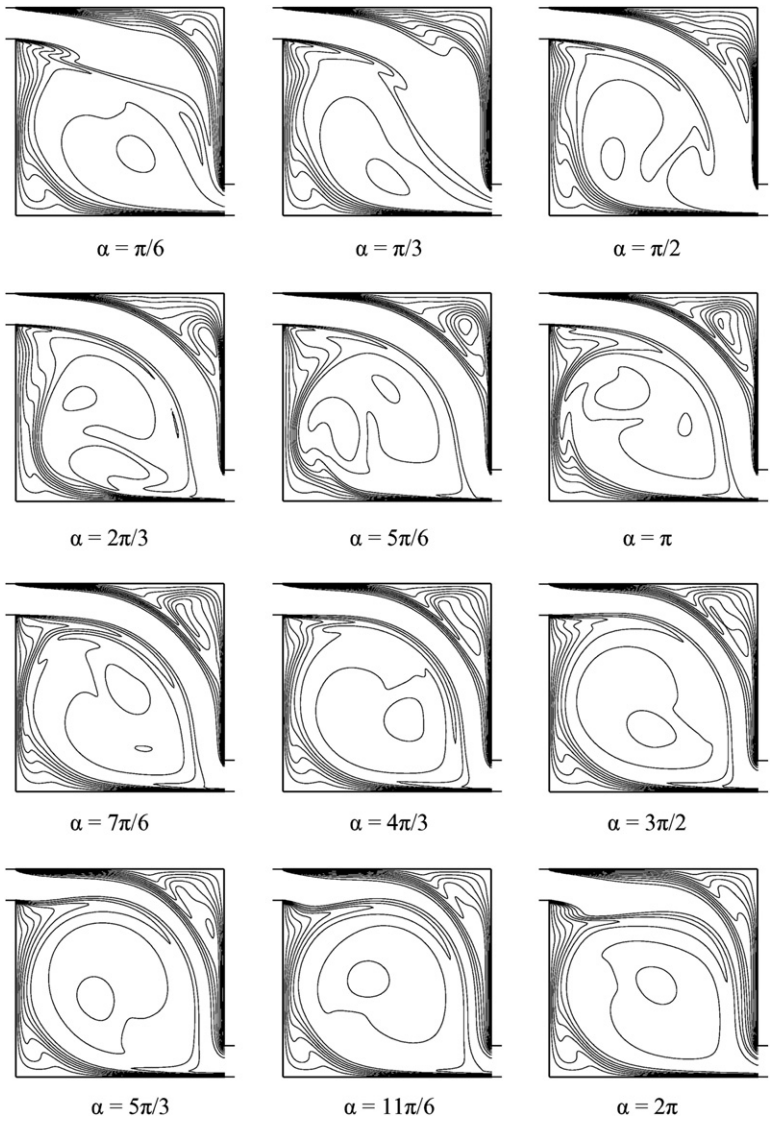

Fig. 6. Periodic evolution of the temperature fields for $St = 0.5$ during the 21st cycle for a $\pi/6$ phase angle increment (contour level increment of 0.05).

and the walls are observed on the left segment of the top wall, the bottom segment of the right wall and the right segment of the bottom wall.

Upon comparing the temperature fields for the five cases that were investigated, the most dramatic changes to the temperature fields were observed for the $St = 1$ case. Similar findings were discussed earlier in relation to the evolving flow field. Interested readers may contact the corresponding author for access to animated videos of the time-dependent flow and thermal fields.

4.4. Transient evolution of the mean Nusselt numbers on the four walls

The transient evolution of the instantaneous mean Nusselt numbers on the four walls are shown in Figs. 7 and 8 for $St = 0.1$ and 10, respectively. The definitions of the instantaneous mean Nusselt numbers on the walls are given as surface integrals of the instantaneous local Nusselt numbers, i.e.

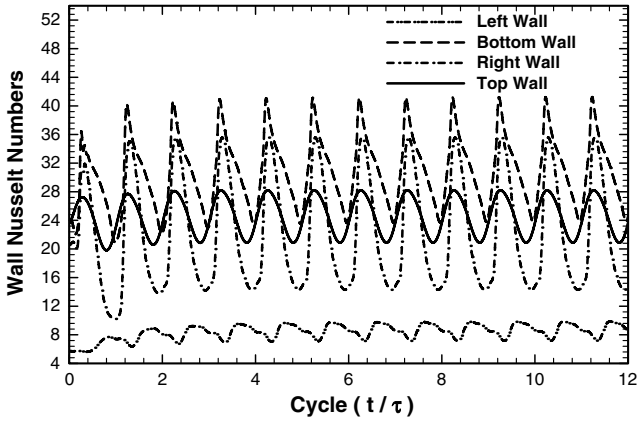

Fig. 7. Transient evolution of the instantaneous mean Nusselt numbers on the four walls for $St = 0.1$.

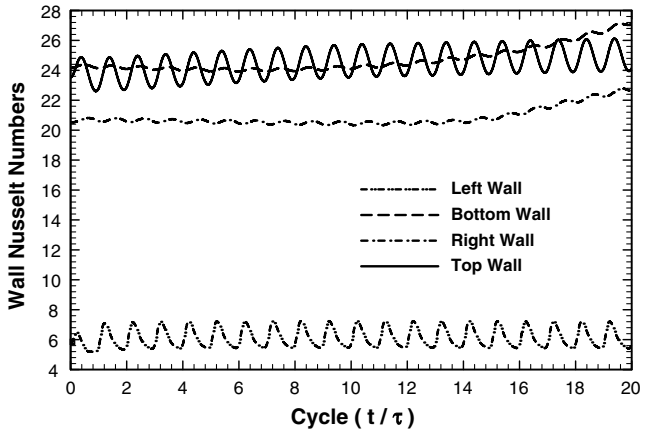

Fig. 8. Transient evolution of the instantaneous mean Nusselt numbers on the four walls for $St = 10$.

$$\overline{Nu_i}(t^*) = \int_0^{\ell_i} Nu_i(s,t^*)\mathrm{d}s = \int_0^{\ell_i} -\frac{\partial \Theta}{\partial n}\bigg|_{\text{wall}} \mathrm{d}s, \tag{8}$$

with the subscript i representing b, l, r and t that correspond to the bottom, left, right and top walls, respectively. Dummy variable s is used to denote the wall coordinate along the walls with length of ℓ_i (1 or $(1-w)$). The normal direction to each wall ($\pm X$ or $\pm Y$) is symbolized with n. For comparison purposes, the mean Nusselt numbers on the four walls under steady state conditions for $Re = 100$, 300 and 500 are summarized in Table 2. It is noted that for the Reynolds numbers listed, the minimum and maximum mean heat transfer rates are generally observed on the left and bottom walls, respectively. The bottom wall exhibits a higher heat transfer rate compared to the top wall, except for the lowest Re studied. As for the variations of the instantaneous mean Nusselt numbers on the walls in Figs. 7 and 8, it is observed that regardless of the Strouhal number, the Nusselt number on the left wall is consistently the lowest among the four walls. This was already discussed above in connection with the presence of two low-speed rotating vortices next to the left wall. For the lowest Strouhal number case ($St = 0.1$) shown in Fig. 7, one can observe that the oscillations of the mean Nusselt numbers on the four walls are easily recognizable. This is due to the long period of oscillation in relation to the convective time scale ($t_{\text{conv}} = H/u_{\text{m}} = St\tau$). In other words, as the inlet velocity oscillates slowly, convection has enough time to transmit the oscillation of the inlet velocity to every point within the cavity. The amplitudes of the oscillations exhibited on the four walls are also marked in comparison to the steady state values for $Re = 300$ in Table 2. For the highest Strouhal number case ($St = 10$) shown in Fig. 8, the time for the fluid to travel from one side of the cavity to another side is greater than the period of the velocity's oscillation. Therefore, the signature of flow oscillation at the inlet port is only observed on the left and top walls of the cavity. The top wall is in the closest proximity of the throughflow that brings in the oscillation information, whereas the left wall also feels the penetration of the throughflow discussed earlier. The amplitudes of oscillations of the Nusselt numbers on the bottom and right walls are heavily damped compared to the low frequency oscillation case of Fig. 7. This can be explained in light of the minimal interaction of the throughflow with these walls because of the frequent presence of the vortices next to them.

Table 2
Mean Nusselt numbers on the four walls under steady state conditions

Re	$\overline{Nu_l}$	$\overline{Nu_b}$	$\overline{Nu_r}$	$\overline{Nu_t}$
100	4.13	14.2	10.1	15.8
300	5.61	22.3	18.3	21.4
500	6.79	30.3	28.0	27.9

4.5. Variation of the overall Nusselt number of the cavity

Another variable utilized to evaluate the heat transfer rate is the total or overall Nusselt number of the cavity. Since all the four walls are active in heat exchange, the total Nusselt number is related to the sum of the individual mean Nusselt numbers ($\overline{Nu_i}$). Therefore, the total Nusselt number of the cavity is defined as

$$\overline{Nu}_{\text{tot}}(t^*) = \frac{1}{4}\sum_i \frac{\overline{Nu_i}(t^*)}{\ell_i}. \tag{9}$$

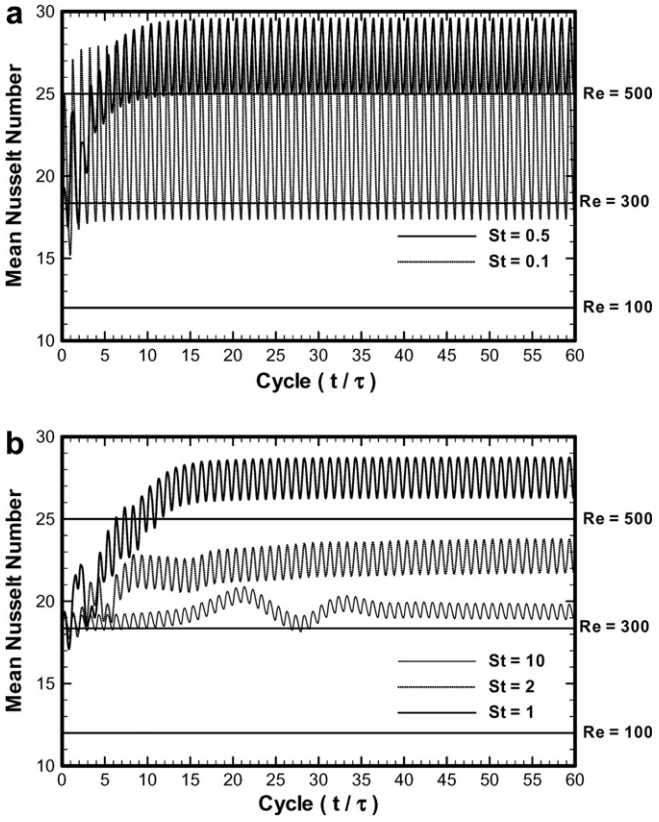

Fig. 9. Transient evolution of the instantaneous total or overall Nusselt number of the system: (a) $St = 0.1$ and 0.5, and (b) $St = 1$, 2 and 10.

The instantaneous total Nusselt number of the cavity for different Strouhal numbers are given in Fig. 9. The two low frequency cases with $St = 0.5$ and 0.1 are shown in Fig. 9a, whereas the cases with $St = 1$, 2 and 10 are shown in Fig. 9b. The periodic nature of the total Nusselt number of the system is consistently maintained regardless of the Strouhal number. The amplitude of oscillation consistently decreases as the Strouhal number is raised covering the low to high frequency cases studied. Except for a short time span during each cycle for $St = 0.1$, heat transfer rate from the cavity is always enhanced in comparison to the steady-state performance of the system for $Re = 300$. For the Strouhal numbers of 0.5 and 1, the instantaneous heat transfer attained after 10 cycles is always above the performance for the steady case with $Re = 500$. This suggests that oscillating the inlet velocity about a Strouhal number of unity when the frequency of oscillation resonates with the convection time scale is the optimum condition for this system.

The values of the average, maximum and minimum overall Nusselt number of the cavity in relation to the Strouhal number are shown in Fig. 10. It is clearly shown that the average value of the instantaneous overall Nusselt number of the system reaches its maximum for a Strouhal number near unity. This suggests that the period of oscillation of the system resonates with the convection time scale of the problem. The amplitude of the overall Nusselt number is observed to decay from 10.6 to 1 as the Strouhal number is increased by two orders of magnitude. It is noteworthy to mention that the dependence of the average, minimum and maximum kinetic energy of the fluid in the cavity in relation to the Strouhal number is very similar to the behavior exhibited in Fig. 10 [19]. These behaviors are clearly linked to the cycle-to-cycle variations of the flow and temperature fields discussed earlier.

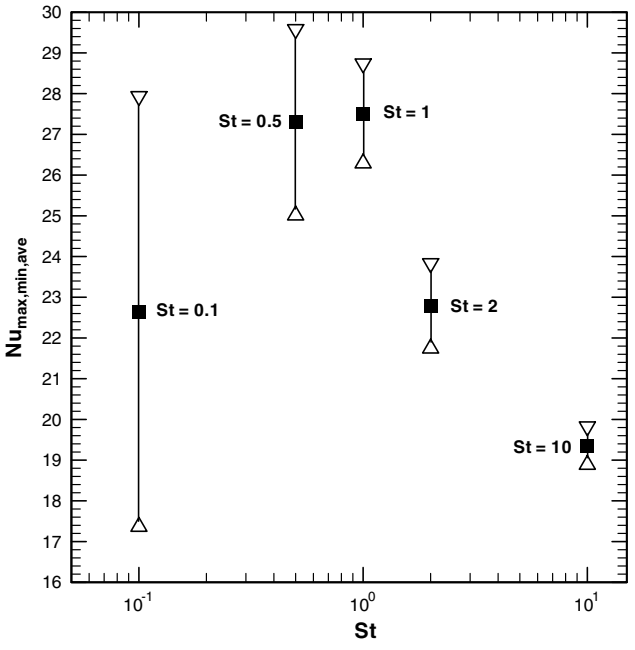

Fig. 10. Dependence of the average, maximum and minimum values of the intantaneous total or overall Nusselt number of the system on the Strouhal number.

5. Conclusions

1. Both the flow patterns and temperature fields in a cavity due to an oscillating velocity at the inlet port reach their respective periodic states after certain time durations. It takes more cycles for the temperature field to reach its periodic state in comparison to the corresponding flow field. For cases with greater Strouhal numbers, it takes more cycles to reach the periodic state.
2. The oscillation of the velocity at the inlet port causes the cyclic growth and decay of the throughflow. The throughflow stream is in constant contact with the CW rotating primary vortex, which in turn interacts with two rotating vortices on the left wall. A CCW rotating vortex at the top right corner also experiences periodic growth and decay.
3. The temperature field is directly affected by the flow field to the extent that it supports minimal heat transfer on the left wall. In contrast, certain segments of the other three walls and the boundary of the throughflow are zones of active heat exchange.
4. For the low Strouhal number of 0.1, the mean Nusselt numbers on the four walls clearly exhibit large amplitudes of oscillation and periodicity. On the other extreme, with $St = 10$, the amplitudes of oscillation are degraded. These behaviors are directly linked to the relation between the period of oscillation and the convection time scale.
5. Regardless of the Strouhal number, heat transfer enhancement in comparison to the performance of the system for the mean Reynolds number is consistently observed. The best heat transfer rate is realized when the Strouhal number is close to unity. This is the case when the period of the incoming stream resonates with the convection time scale.

References

[1] T.-H. Hsu, P.-T. Hsu, S.-P. How, Mixed convection in a partially divided rectangular enclosure, Numer. Heat Transfer, Part A 31 (1997) 655–683.
[2] T.H. Hsu, S.G. Wang, Mixed convection in a rectangular enclosure with discrete heat sources, Numer. Heat Transfer, Part A 38 (2000) 627–652.
[3] S.Z. Shuja, B.S. Yilbas, M.O. Iqbal, Mixed convection in a square cavity due to heat generating rectangular body. Effect of cavity exit port locations, Int. J. Numer. Meth. Heat Fluid Flow 10 (2000) 824–841.
[4] S.Z. Shuja, B.S. Yilbas, M.O. Budair, Natural convection in a square cavity with a heat generating body: entropy considerations, Heat Mass Transfer 36 (2000) 343–350.
[5] A.M.C. Chan, P.S. Smereka, D. Giutsi, A numerical study of transient mixed convection flows in a thermal storage tank, J. Solar Energy Eng. 105 (1983) 246–253.

[6] A. Bouhdjar, A. Benkhelifa, A. Harhad, Numerical study of transient mixed convection in a cylindrical cavity, Numer. Heat Transfer, Part A 31 (1997) 305–324.
[7] K.O. Homan, S.L. Soo, The steady horizontal flow of a wall jet into a large-width cavity, J. Fluid. Eng. 120 (1998) 70–75.
[8] A. Omri, S.B. Nasrallah, Control volume finite element numerical simulation of mixed convection in an air-cooled cavity, Numer. Heat Transfer, Part A 36 (1999) 615–637.
[9] G.M. Rosengarten, M. Behnia, G. Morrison, Some aspects concerning modelling the flow and heat transfer in horizontal mantle heat exchangers in solar water heaters, Int. J. Energy Res. 23 (1999) 1007–1016.
[10] A. Bouhdjar, A. Harhad, Numerical analysis of transient mixed convection flow in storage tank: influence of fluid properties and aspect ratios on stratification, Renew. Energy 25 (2002) 555–567.
[11] S. Singh, M.A.R. Sharif, Mixed convective cooling of a rectangular cavity with inlet and exit openings on differentially heated side walls, Numer. Heat Transfer, Part A 44 (2003) 233–253.
[12] S.M. Saeidi, J.M. Khodadadi, Forced convection in a square cavity with inlet and outlet ports, Int. J. Heat Mass Transfer 49 (2006) 1896–1906.
[13] A.T. Patera, B.B. Mikic, Exploiting hydrodynamic instabilities: resonant heat transfer enhancement, Int. J. Heat Mass Transfer 29 (1986) 1127–1138.
[14] M. Greiner, An experimental investigation of resonant heat transfer enhancement in grooved channels, Int. J. Heat Mass Transfer 34 (1991) 1383–1391.
[15] T. Nishimura, K. Kunitsugu, A.M. Morega, Fluid mixing and mass transfer enhancement in grooved channels for pulsatile flow, Enhanc. Heat Transfer 5 (1998) 23–37.
[16] S.V. Patankar, Numerical Heat Transfer and Fluid Flow, Hemisphere Pub. Co., Washington, DC, 1980.
[17] T. Hayase, J.A.C. Humphrey, R. Grief, A consistently formulated QUICK scheme for fast and stable convergence using finite-volume iterative calculation procedures, J. Comp. Phys. 98 (1992) 108–118.
[18] X. Shi, Forced and natural convection heat transfer within enclosures with fixed and moving fins and partitions, Ph.D. Thesis, Department of Mechanical Engineering, Auburn University, 2003.
[19] S.M. Saeidi, Fluid flow and heat transfer in cavities with inlet and outlet ports: effect of flow oscillation and application to design of microvalves, Ph.D. Thesis, Department of Mechanical Engineering, Auburn University, 2005.
[20] C.J. Freitas, Perspective: selected benchmarks from commercial CFD codes, J. Fluid. Eng. 117 (1995) 208–218.
[21] J.A. Walter, C.-J. Chen, Visualization and analysis of flow in an offset channel, J. Heat Transfer 114 (1992) 819–826.